Spatiotemporal wicking dynamics: The effects of pillar height, density, and anisotropic geometries

John Bal, Krishnan S.R. Manoharan, and Shawn A. Putnam
Department of Mechanical and Aerospace Engineering
University of Central Florida, 12760 Pegasus Drive, Orlando, FL, USA, 32816
Email: shawn.putnam@ucf.edu

Abstract—Asymmetric microstructures are of particular interest to many technical fields. Such structures can produce anisotropic flow-fields, which, for example, can be used to control heat and mass transport processes. Anisotropic wicking structures can now be systematically engineered with unique micro-pillar geometries and spatial pillar-placement distributions. Such asymmetric wicking structure designs are of particular interest to the thermal management community due to need to cool heterogeneous materials with specific heat load configurations. In this study, asymmetric half-conical micropillars have been fabricated utilizing two-photon polymerization. Macroscopic characterization of anisotropic flow-field velocities is performed via high-speed videography. High-speed thin-film interferometry and microscopic side-angle videography are also used to characterize the microscale evolution of meniscus curvature during inter-pillar wicking. The wicking velocity is observed to be directly proportional to both the meniscus curvature and the crosssectional area of the micro-pillars (normal to the flow). An anisotropic hemiwicking model is also described with comparisons to experimental data. The hemiwicking model predicts the macroscopic wicking behavior (within 20% or less) for the relatively broad range of pillar geometries and pillar spacing configurations. These anisotropic flow-field predictions can help engineers design the next-generation of micro-structured heat sinks, fluid-based sensors and chemical harvesting systems.

Keywords—hemiwicking, anisotropic, microstructure, meniscus, spatiotemporal, videography, interferometry, wetting

NOMENCLATURE

- r radius (m)
- $D_{\rm I}$ interface diffusivity (m²/s)
- C_d drag coefficient (unitless)
- C_{d0} drag number (unitless)
- δf force per unit cell width normal to the flow (N/m)
- s pillar spacing (m)
- h pillar height (m)
- f roughness factor
- x_0 meniscus extension (m)
- ℓ length (m)
- h meniscus height (m)
- S solid-liquid structure factor (unitless)
- v velocity (m/s)
- K_{\diamond} solid-liquid surface texture (m)
- w fringe spacing (m)
- RA rapid ascent
- SC sluggish climb
- StS side-to-side

Greek symbols

- α pillar skew angle (degrees)
- δ_0 absorbed thin-film thickness (m)
- γ fluid surface tension (N/m)
- θ meniscus or contact angle (degrees)
- κ meniscus curvature (m⁻¹)
- μ dynamic viscosity (Pa·s)
- density (g/cm³)

I. INTRODUCTION

Recent advancements in microelectronics have increased the need for thermal management systems capable of high heat flux dissipation within significant spatial constraints. These spatial constraints and high heat flux conditions have led to renewed interest in novel microscale heat transfer techniques. Techniques, including jet-impingement, spray cooling, and microchannel cooling, offer vastly improved heat flux performances for small surface areas compared to traditional methods [1,2]. The inclusion of micro-and nano-scale surface features facilitate further enhancements in the cooling performance. Superlyophilic surface texturing is of particular interest because such surface structures can act as a fluid pump, transporting (or spreading) a fluid across a material by coordinated pillar micro-pumping of a fluid thin-film (or liquid meniscus), with applications in thin-film evaporation, as well as pool, flow, and thin-film boiling. Thus, tailored, anisotropic wicking arrays (i.e., hemiwicks) facilitate the potential to enhance active and passive phase-change cooling methods. The recent focus on physically and chemically microstructured surfaces has proven to be beneficial for delaying wall dry-out in critical heat flux conditions, as well as maintaining a steady meniscus for thin-film evaporation [3,4]. Moreover, the progress in materials science and manufacturing makes such micro- to nano-engineered surfaces applicable to both high- and low-temperature environments.

Micro- and nano-structured surfaces can act a fluid pump by utilizing spatiotemporal capillary pressures to propel a fluid beyond its intrinsic meniscus extension, effectively creating a superlyophilic surface [5] Such self-pumping fluid motion, occurring in the Stokes flow regime, is termed "hemiwicking". Asymmetric microstructures have come into focus as an especially effective method of tailoring a cooling system to pump fluids through specific heating configurations by utilizing complex flow patterns. Understanding the complicated intermolecular and interfacial interactions that accompany a hemiwicking flow is necessary for predicting and optimizing the performance of self-regulating cooling technologies.

Recently, Krishnan et al. investigated the fluid propagation velocity in hemiwicking arrays of cylindrical micro-pillars by scaling the Laplace pressure within the fluid using the steady-state meniscus extension (x_0) developed at the end of the wicking array [7]. Kim et al. investigated the microscopic propagation front between two pillars and found two distinct regimes separated by the dominant driving force: directly after the fluid reaches a pillar, the front propagation is dominated by surface energy minimization as the fluid climbs the pillar, while at later time-scales (after the primary fluid rise) the propagation is dominated by Laplace pressures also due to a curved menisci [8].

Perpendicular anisotropic droplet wetting via the use of surface ridges has been exhibited [9]. Local physical barriers prevented droplet wetting in one direction while allowing wetting in the perpendicular direction. Triangular structures have anisotropic qualities due to a meniscus instability between the flat faces and sharp edges. Increased stability against the flat face of the pillar leadd to anisotropic wetting or unidirectional wetting, depending on pillar spacing [10]. One-way wicking in open microchannels has been shown to be dependent on Laplace pressure differences via asymmetric topography [11]. The current study looks to improve upon these results by looking at the individual temporal and spatial evolution of the meniscus curvature via interferometry to study the microscopic differences in Laplace pressures (depending on the wicking direction) across an asymmetrically structured surface.

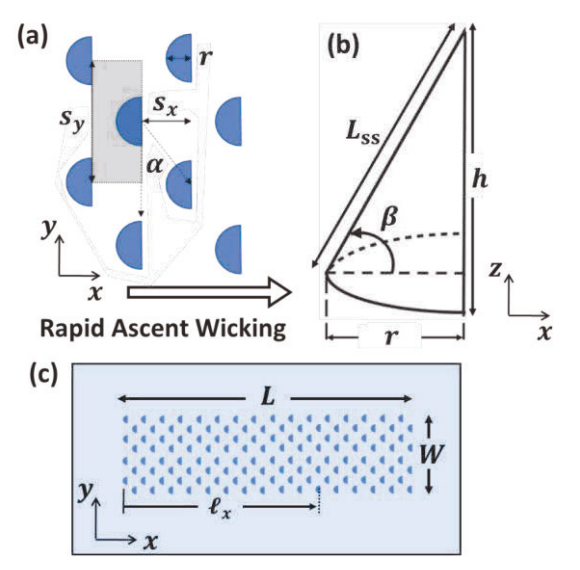


Fig. 1. Schematic illustration of the half-conical (anisotropic) geometries and spacing configurations. **(a)** Pillar spacing configuration, where the gray box signifies the unit cell of the wicking structure. **(b)** Geometry of an individual pillar. **(c)** Fabricated wicking structure on Si, where L=4 mm and W=1 mm. The fastest wicking direction (called Rapid Ascent wicking) is depicted for both (a) and (b).

II. EXPERIMENTAL DETAILS

A. Fabrication of Anisotropic Hemiwicking Structures

The samples were fabricated on Nanoscribe Pro GT laser lithography system capable of two-photon polymerization. Pillars were deposited on silicon (Si) wafers with a thickness of 0.50 mm. After nanoscribe fabrication, a thin film of Al_2O_3 (thickness $\sim\!150$ nm) was deposited onto the hemiwicking samples to obtain both a uniform surface energy distributions and rigid wicks.

Fig. 1 shows the sizing and spacing parameters of the half-conical wicking structures used in this study. In correlation with the half-conical pillar geometries, the preferred (or more rapid) wicking direction is called 'Rapid Ascent' (RA) wicking; whereas the non-preferred (or slower) wicking direction is called 'Sluggish Climb' (SC) wicking. Fig. 1 illustrates the RA wicking direction with respect to the fabricated half-conical pillar geometry. Fig. 2 provides SEM images of the half-conical pillars for a few different samples. SEM measurements were performed to confirm the spatial parameters of the studied wicking samples. Table 1 in the Appendix lists the geometrical properties and

spacing configurations of the hemiwicking samples used in this study. The measured pillar heights (h_m) by SEM are listed in Table 1, along with the corresponding set-point pillar heights $(h_{\rm SD})$ used by the Nanoscribe instrumentation.

Fig. 3 provides high-speed camera images of the half-conical pillars and their interactions with wicking fluids. The width (W) and length (L) of the studied hemiwicking arrays were 1 mm and 4 mm, respectively. The array skew angles (α) were either 0° or 45°. The base radius of the pillars (r) were either 10 µm or 15 µm. The half-cone angle (β) ranged from 69° to 83°. The pillar heights (h) varied from 39 µm to 102 µm (see, Table 1). The side slope length is given by $L_{ss}=r^2+h^2$. These geometrical parameters are used to calculate the corresponding roughness factor of the wicking array.

The roughness factor (f) is a dimensionless proportion that relates the actual surface area to the projected surface area of the pillar array. For pillar arrays of symmetric, vertical cylinders, $f = 1 + \frac{2\pi rh}{s_x s_y}$. Whereas, for the half-conical pillars,

$$f = 1 + \frac{rh + \frac{\pi r L_S}{2}}{s_y s_x}.$$
 (1)

In this work, the fabricated roughness factors of the half-conical pillars ranged from 1.34 to 2.58 (see, Table 1).

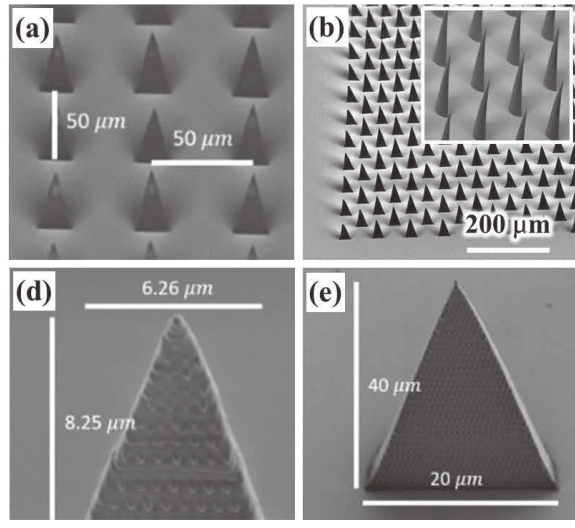


Fig. 2. SEM images of the anisotropic, half-conical hemiwicking samples fabricated at ORNL in the Center for Nanophase Material Sciences Nanofabrication. The images were acquired using a Merlin Phenom SEM at ORNL: **(a)** sample H, **(b)** sample F, **(d)** sample G (pillar-tip), and **(e)** sample A. The SEM *x*- and *y*-scales are not identical due to SEM imaging at an angle.

B. Scaling Analysis: Predicting the Velocity for Anisotropic Hemiwicking Flow

In wicking arrays with asymmetric pillar geometries and pillar distributions, the static meniscus extension as well as the temporal evolution of meniscus extension are expected to differ depending on wicking direction relative to the asymmetric pillar structure. In our previous hemiwicking studies with cylindrical pillars, we derived a simple analytical solution for the wicking

velocity based on a force (or energy) balance between the drag force (F_d) and the driving force (F_w) for wicking. The drag force is in the creeping (Stokes) flow regime because the maximum Reynolds numbers for hemiwickinig are $Re_d < 1$.

The driving force for wicking is due to capillary action (and/or imbibition) and is directly proportional to the curvature of the liquid meniscus. This driving force was approximated based on the Laplace pressure in the wicking front of the liquid meniscus. In particular, the Laplace pressure scaled as the product of the fluid's surface tension (γ) and the curvature of the liquid meniscus (κ) – i.e., $P_{\text{Laplace}} \sim \gamma \kappa$. For cylindrical or rectangular pillars of height (h), we approximated the meniscus curvature $(\frac{d^2 h}{dx^2})$ as $\kappa \sim \frac{h}{x_0^2}$, where x_0 is the meniscus extension, h is the meniscus height. If h = h, then the pillars are fully wetted. We also note that x_0 is not the maximum length that the liquid meniscus can extend from a vertical structure. The meniscus thin-film (or near zero curvature) region of the liquid meniscus extends to lengths greater than the steady-state value of x_0 . This concept is illustrated by comparing the steady-state fringes in Fig. 3a with the transient meniscus in Fig. 3c.

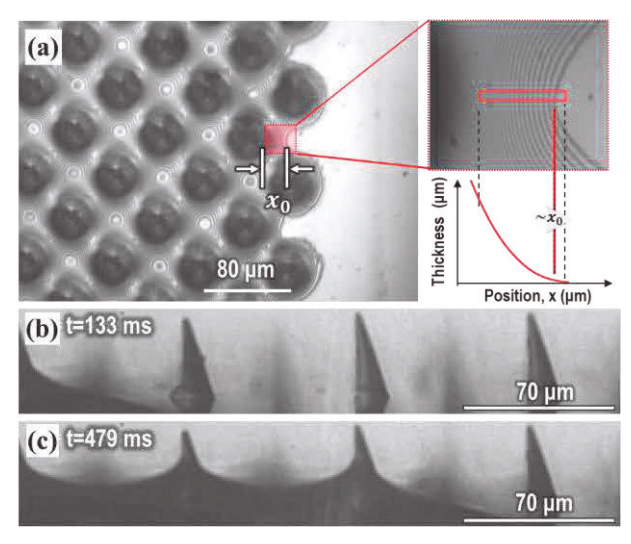


Fig. 3. High-speed images of hemiwicking with anisotropic pillar arrays. (a) High-speed interferometry image of sample G using the interferometry (fringe) analysis setup for characterizing both the meniscus curvature (κ) and meniscus extension (x_0). The inset image in (a) is a magnified view of the fringe spacing and corresponding meniscus profile, where x_0 is measured at the end of 'Sluggish-Climb' (SC) hemiwicking process during steady-state evaporation. (b, c) Sideview high-speed videography images of the propagation of the liquid meniscus (sample O). The side-view image shows the spatiotemporal meniscus profile during SC wicking at the edge of the wicking array.

As depicted in Fig. 3, anisotropic pillars produce anisotropic meniscus curvatures. Hence, anisotropic pillars yield different geometrical profiles (or meniscus view-factors) relative to the direction of hemiwicking flow. For example, from a back focal perspective (bfp) during rapid ascent wicking, the meniscus curvature is estimated as $\kappa_{\rm bfp}^{\rm RA} \approx h/x_0(x_0 + \Delta x)$. Whereas, from the forward focal perspective (ffp), $\kappa_{\rm ffp}^{\rm RA} \sim h/x_0^2$. The denominator terms $x_0(x_0 + \Delta x)$ or x_0^2 in $\kappa_{\rm bfp}^{\rm RA}$ and $\kappa_{\rm ffp}^{\rm RA}$ (respectively) are due the difference in the perceived pillar

height: $h_p = \frac{hx_0}{x_0 + \Delta x}$. This scaling for h_p is based on the simple optics relationship between the perceived height of an object at a distance, where we use x_0 as the effective reference point and $\Delta x = C_1 r$ as an extra viewing distance proportional to the base radius of the half-conical pillars.

The drag force for these half-conical (anisotropic) wicking arrays is calculated following the same derivation procedure in Ref. [7]. For the creeping (Stokes) flow regime, the drag force is the same for both the +x (RA) and -x (SC) wicking directions. For wicking along the y-axis, the drag force is again axis-symmetric. However, if the drag coefficient (C_d) is a constant, then the drag force along the y-axis is a factor of 2 less than that for the x-axis because of the reduction frontal area (e.g., $A_F^{\pm y} = rh/2$ and $A_F^{\pm x} = rh$). For reference, the frontal area for cylindrical pillars is axis-symmetric: $A_F^{\rm cyl} = 2rh$. Nevertheless, if C_d is isotropic for the half-conical pillars, then the anisotropic drag force due to the pillars (per unit cell width normal to the flow) is

$$\delta f_d^{\pm x} = \frac{1}{2} \rho v^2 C_d \left(\frac{hr}{s_x s_y} \right) \ell_x , \qquad (2)$$

$$\delta f_d^{\pm y} = \frac{1}{2} \rho v^2 C_d \left(\frac{hr/2}{s_x s_y} \right) \ell_y , \qquad (3)$$

where ℓ_x and ℓ_y represent the distances the meniscus front has propagated in the x- and y-directions (respectively) with maximum values of $\ell_x = L$ and $\ell_y = W$. In this context, for example, the number of wicked pillars (N_p) and the net frontal drag area (per unit cell width normal to the x-axis flow) are $N_p = (1/s_x)\ell_x$ and $\delta A_{d,\text{net}}^{\pm x} = N_p(A_F^{\pm x}/s_y) \approx (hr/s_x s_y)\ell_x$.

In Eqs. (2) and (3), drag coefficients of the form $C_d = C_{d0}/\text{Re}_d$, where a drag number of $C_{d0} \approx 24$ can be assumed because of the observed wicking speeds are in the creeping (Stokes) flow regime (Re < 1). We note that past work with cylindrical pillars yielded $C_{d0} \cong 95$ using ethanol, water, and FC70 wicking fluids and $\text{Re}_d = 2\rho vr/\mu$. If we consider anisotropic drag coefficients and maintain the previous convention for approximating the characteristic length, then for the half-conical pillars: $\text{Re}_d^{\pm x} = \rho vr/\mu$ and $\text{Re}_d^{\pm y} = \rho vr/2\mu$. In result, $C_d^{\pm x} = C_d^{\pm y}/2$ and Eqs. (2) and (3) end up being mathematically identical.

Eqs. (2) and (3) do not account for the drag associated with the flat wall surface. Accounting for the drag from the flat wall without pillar structures, Eqs. (2) and (3) become

$$\delta f_d^{\pm x} = \frac{\rho v^2}{2} \left[C_d^{\text{pillar}} \left(\frac{hr}{s_x s_y} \right) + C_d^{\text{wall}} \left(1 - \frac{\pi r^2 / 2}{s_x s_y} \right) \right] \ell_x, \quad (4)$$

$$\delta \mathbf{f}_{d}^{\pm y} = \frac{\rho v^{2}}{2} \left[C_{d}^{\text{pillar}} \left(\frac{hr/2}{s_{x} s_{y}} \right) + C_{d}^{\text{wall}} \left(1 - \frac{\pi r^{2}/2}{s_{x} s_{y}} \right) \right] \ell_{y}, \quad (5)$$

where the wall drag coefficients are of the form: $C_d^{\rm wall} = 1.33/\sqrt{{\rm Re}_L}$ and $C_d^{\rm pillar} = C_{d0}/{\rm Re}_d$. We note that the measured wicking velocities typically range from 1 mm/s to ~30 mm/s. Correspondingly, $C_d^{\rm pillar}/C_d^{\rm wall} \gtrsim 30$; therefore, the wall drag effects can be neglected (as done previously). Nevertheless, to

include the flat wall effects, Eqs. (4-5) can be slightly simplified via scaling the wall drag coefficient in terms of the pillar drag coefficient with $C_d^{\text{wall}} \sim C_d^{\text{pillar}} \times (r^2/s_x s_y)$.

Due to the anisotropic pillar geometries, the net driving force for wicking (F_w) is also anisotropic. Thus, relative to wicking in the +x, -x, and $\pm y$ propagation directions – as outlined in Fig. 1, the anisotropic wicking force (per unit cell width normal to the flow) can be derived as:

$$\delta f_w^{+x} = \gamma \left(\frac{h}{x_0^2} \right) \left(h \frac{r}{s_y} \right), \tag{6}$$

$$\delta f_w^{-x} = \gamma \left(\frac{h}{x_0(x_0 + C_1 r)} \right) \left(h \frac{r}{s_y} \right), \tag{7}$$

$$\delta f_w^{\pm y} = \gamma \left(\frac{h}{x_0(x_0 + C_1 r)} \right) \left(h \frac{r/2}{s_x} \right), \tag{8}$$

where the +x, -x, and $\pm y$ subscripts correspond to meniscus propagation in the Rapid Ascent (RA), Sluggish Climb (SC), and Side-to-Side (StS) directions. To account for the increased wicking speeds with staggered pillar placements (e.g., $\alpha = 45$) in comparison to simple cubic ($\alpha = 0^{\circ}$, $s_x = s_y$) pillar placements, Eqs. (6-8) can be simply divided by $\cos \alpha$.

In Eqs. (6-8), the first parentheses contribution represents the effective meniscus curvature ($\kappa_{\rm eff}$). As discussed previously, the provided functional forms for κ_{eff} account for the perceived pillar height by the propagating meniscus when viewed at a distance of x_0 or $(x_0 + r)$ from the apex of the pillar. The second parentheses contribution accounts for the different frontal areas (per unit cell width normal to the flow) that the 'meniscus is actively using to drive the hemiwicking flow'. In our past work, we scaled this second term to be strictly the pillar height (h) – rather than an area-weighted pillar height (e.g., $h \times r/s_v$), where, again, this weighting is based on the effective frontal pillar area seen by the meniscus (per unit cell width normal to the flow). We note that implementation of an areaweighted pillar height to our recent studies and analysis with cylindrical pillars results in an effective reduction in C_{d0} by factor of 4 to 6 (e.g., $h \rightarrow h \times 2r/s_y \approx h/4$ - h/6). Thus, drag coefficients with corresponding C_{d0} values in the range of that expected -- i.e., $C_{d0} \simeq 24$ for creeping (Stokes) flow.

Neglecting the drag from flat wall surface, a force balance between δf_d (Eqs. (2-3)) and δf_w (Eqs. (6-8)) results in the corresponding wicking velocities:

$$\mathbf{v}^{+x} = \frac{2}{c_{d0}} \left(\frac{\gamma}{\mu} \right) \left(\frac{1}{x_0^2} \right) \left(\frac{hrs_x}{\ell_x \cos \alpha} \right), \tag{9}$$

$$\mathbf{v}^{-x} = \frac{2}{c_{d0}} \left(\frac{\gamma}{\mu} \right) \left(\frac{1}{x_0 (x_0 + c_1 r)} \right) \left(\frac{h r s_x}{\ell_x \cos \alpha} \right), \tag{10}$$

$$\mathbf{v}^{\pm y} = \frac{1}{c_{d0}} \left(\frac{y}{\mu} \right) \left(\frac{1}{x_0 (x_0 + c_1 r)} \right) \left(\frac{h r s_y}{\ell_y \cos \alpha} \right). \tag{11}$$

We note that Eqs. (9-11) breakdown as the pillar spacing decreases to values comparable to (or less than) the pillar base radius (i.e., $s_x \le r$ or $s_y \le 2r$, depending on the flow direction). Therefore, as done previously, to account for this packed bed limit we can replace s_x and s_y with $(s_x - r)$ and $(s_y - 2r)$,

respectively. We also note that in previous work we multiplied the velocity predictions by $(f-1)^{1/2}$ as a refinement for the one-dimensional drag.[7] However, in this work, we have removed this 'refinement' because it is accounted for via the scaling for an area-weighted pillar height (e.g., $h \times r/s_v$).

Now, Eqs. (9-11) can be compactly rewritten to emphasize the wicking velocity in terms of (i) a solid-liquid Structure factor $(S = K_o/\ell)$ and (ii) a capillary velocity $(v_{Ca} = \gamma/\mu)$. In this regard, Eqs. (9-11) can be rewritten as

$$v = \frac{s}{c_{d0}} v_{Ca} = \frac{1}{c_{d0}} \frac{\kappa_o}{\ell} \left(\frac{\gamma}{\mu} \right), \tag{12}$$

where $C_{d0} \sim 24 = C_{d0}^{\text{Stokes}}$ and K_{\circ} is the anisotropic solid-liquid surface texture of the wicking array.

We stress that the capillary velocity in Eq. (12) is unique to the wicking fluid. Moreover, v_{Ca} represents the maximum theoretical wetting velocity for a fluid in instantaneous contact with a ridged body - i.e., wetting in the absence of irreversible energy loss. However, we typically observe upper-limit liquid wetting velocities within $0.5 \text{ m/s} \lesssim v_0 \lesssim 3 \text{ m/s}$, correspondingly for both (i) a wide variety of different flat, non-textured solid surfaces (e.g., Au, Si, SiO₂, Al₂O₃, PDMS, graphene, Teflon, etc.) and (ii) several different liquids (e.g., water, ethanol, Isopropanol, Isooctane, FC70, etc.). Thus, usually v_0 is an order of magnitude less than v_{Ca} (e.g., v_{Ca} for isopropanol and ethanol is 25.1 m/s and 24.9 m/s, respectively). Also, because our wicking model is based mainly on scaling analysis, a more appropriate value for C_{d0} (rather than $C_{d0} \sim 24$) should be determined from many experiments, using not only multiple fluids (i.e., fluids with distinctive v_{Ca} values), but also a diverse set of wicking structures (i.e., wicks with isotropic and anisotropic surface textures).

The surface texture (K_0) in Eq. (12) has units of length (m), analogous to the units for surface roughness in tribology and materials science. However, this surface texture couples the spatial fluid wetting characteristics (i.e., meniscus curvature) with the wicking array packing structure and pillar geometry. Hence the name, solid-liquid surface texture. With respect to the wicking direction (relative to the wicking texture), the surface textures for the anisotropic, half-conical wicking arrays are

$$K_{\circ}^{+x} = \frac{2}{\cos \alpha} \frac{hr(s_x - r)}{x_0^2},$$
 (13)

$$K_{\circ}^{-x} = \frac{2}{\cos \alpha} \frac{hr(s_{x}-r)}{x_{0}(x_{0}+c_{1}r)},$$
(14)

$$K_{\circ}^{\pm y} = \frac{1}{\cos \alpha} \frac{hr(s_y - 2r)}{x_0(x_0 + c_1 r)},\tag{15}$$

where, again, the +x, -x, and $\pm y$ subscripts correspond to wicking in the Rapid Ascent (RA), Sluggish Climb (SC), and Side-to-Side (StS) directions. For reference, the surface texture for cylindrical pillars with symmetric pillar placements (i.e., cubic unit cells) should be

$$K_{\circ}^{\text{cyl}} = \frac{2r}{s_{\chi}} \frac{2hs_{\chi}(s_{\gamma}-2r)}{x_{0}^{2}}$$
 (16)

This revised solid-liquid surface texture accounts for the areaweighted pillar height (relative to the flow cross-section) and is consequently a factor $2r/s_x$ less than that provided in Ref. [7].

These predictions for the anisotropic wetting velocity are compared to our experimental results in Sec. III. We note that in all subsequent discussion and data dissemination that the +x and -x sign convention will not be used. To avoid misuse of positive and negative flow directions, the Rapid Ascent (RA) and Sluggish Climb (SC) terms will be referenced instead and +x will corresponding to the flow direction.

C. Experimental Methods

As discussed in the previous sections, hemiwicking motion is expected to be dependent on the orientation of the wetting plane (or meniscus contact line) relative to geometrical orientation of the wicking structures. Previously, in Sec. IIB, we referred to this concept in terms of a meniscus view-factor. Moreover, vis-à-vis Eqs. (2-15), we hypothesized how the hemiwicking velocity (or propagation speed of the meniscus front) depends on scaling analysis expressions for both (i) the fluid dynamic drag and (ii) the curvature of the liquid meniscus. To confirm these predictions, high-speed videography is used to capture the spatiotemporal motion of propagating liquid meniscus in the hemiwicking array for the different wicking configurations. Most commonly we used videography frame rates within 1000 ≤ **fps** \leq 10,000. The following describes the experimental techniques and data analysis methods for characterizing the hemiwicking flow-fields with high-speed imagery.

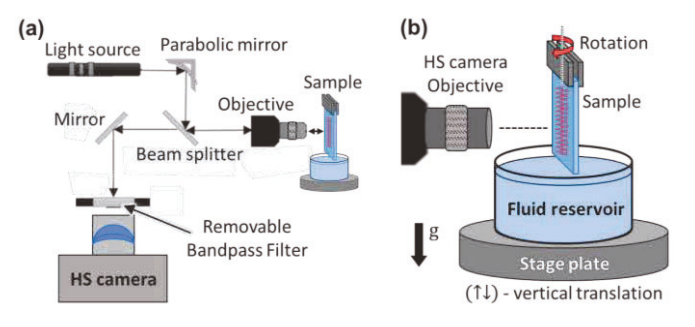


Fig. 4. Optical setup for contemporary videography and interferometry analysis during vertical hemiwicking experiments. **(a)** High-speed (HS) videography optics with removable bandpass filter. Imaging with the bandpass filter facilitates our HS interferometry (fringe) analysis, whereas contemporary HS videography is conducted without the bandpass filter. **(b)** Schematic illustration of the wicking configuration, where the reservoir stage is displaced upward (against gravity) until fluid reservoir pool is in contact with the first row of the pillar array, initiating the wicking process. The sample holder can be rotated 90° for both top-view (shown) and side-view imaging experiments.

Fig. 4 schematically depicts the high-speed interferometry and contemporary videography techniques. Isopropanol (IsoP) and ethanol (EtOH) were the primary fluids studied in this work. The corresponding capillary velocities for ethanol and isopropanol are ~20 m/s and ~12 m/s, respectively. As shown in Fig. 4, the hemiwicking samples are mounted above the fluid reservoir pool for studies in the vertical hemiwicking configuration. Vertical hemiwicking corresponds to both fluid wicking against gravity and fluid wicking parallel with the

surface normal of the fluid pool reservoir. After vertical mounting and alignment of the imaging equipment, the reservoir was translated up on the reservoir stage until the fluid pool was in contact with the first row of pillars. The macroscopic wicking front was then recorded and analyzed for determination of the spatiotemporal meniscus velocity and meniscus curvature. Broadband (white) light or monochromatic (454 nm) laser light are used for illumination sources. To optimize the light collimation a parabolic mirror is used before the 50-50 UV fused silica beam splitter. Light is sent through the long-working distance microscope objective (50× for interferometry analysis and 2×-50× for videography).

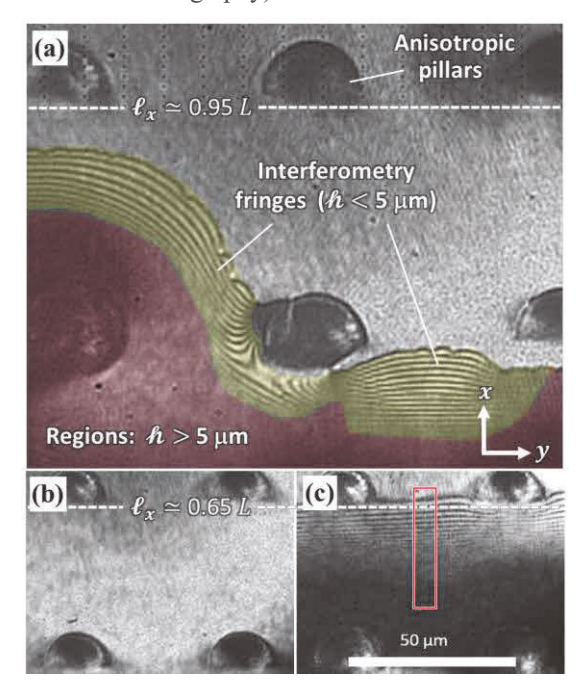


Fig. 5. Spatiotemporal interferometry data for sample H during Sluggish Climb (SC) hemiwicking. (a) Data showing the non-uniform meniscus profile for hemiwicking near the end of the pillar array (e.g., dashed horizontal line: $\ell_x \approx 0.65~L$). Interferometry fringes are not distinct in regions of high meniscus curvatures (or thick menisci regions: $\hbar \gtrsim 5~\mu m$). (b) Inter-pillar interferometry image before hemiwicking in a central region of wicking array ($\ell_x \approx 0.65~L$, $\ell_y \approx 0.5~W$). (c) Interferometry image after a time elapse of $\Delta t \simeq 10~ms$ (b \rightarrow c: uniform leading edge). The red box is the ROI for fringe analysis.

Fig. 5 shows snapshots of the spatiotemporal evolution of the fringe pattern generated by the moving meniscus front during a wicking experiment using the interferometry setup. This dynamic interferometry technique uses the same high-speed camera to capture the distribution of interferometry fringes as a function of time. This interferometry data is for hemiwicking in an interior region of interest. ImageJ subroutines and custom MATLAB and LabView codes were also used for spatiotemporal grayscale edge detection and fringe analysis [12,13]. The interferometry technique is described in detail in Ref. [12]. We note that as the meniscus front (or contact line) propagates from pillar to pillar that the fringe pattern changes due to changes in the meniscus curvature (or thickness distribution of the hemiwicking fluid). ImageJ, MATLAB, and LabView codes are used to analyze the videos with and without interference fringes.

For fringe and side-angle analysis, ImageJ was frequently used to mask and rotate images. Data collected included the temporal evolution of the contact angle, meniscus profile, and meniscus extension between pillars, the fluid wicking over the entire wicking array (via 2× magnification), and fluid wicking in specific regions of interests (e.g., at inception, array side-columns, interior pillars, and the end pillars – via >2× magnification).

The correlation between the interferometry (fringe) distribution and the fluid thickness first requires calculation the of the meniscus curvature profile. The spatiotemporal fringe distribution is related to the slope (or apparent contact angle) distribution by

$$\theta(x, y, t) = \frac{90}{\pi} \frac{\lambda/n}{w(x, y, t)},\tag{17}$$

where θ is expressed for units of degrees, the fringe spacing (w) is the distance between two consecutive light (or dark) fringes, λ is the wavelength of light, and n is the index of refraction of the fluid at λ .

Eq. (17) shows that the contact angle is inversely proportional to the fringe spacing. The interferometry images in Figs. 3 and 5 illustrate this relationship – e.g., the smallest fringe spacings are always near the pillar walls, whereas the largest fringe spacings

are either (i) at the leading edge of the meniscus front or (ii) at menisci trough locations between the wetted pillars. Nevertheless, measurements of w(x, y, t) yield $\theta(x, y, t)$, which can then be used to generate $\hbar(x, y, t)$. For example, a spatiotemporal contour of the fluid thickness distribution can be iteratively calculated with

$$h_{i+1}(x_{i+1}, t) = w(x_i, t) \tan \theta(x_i, t) + h_i(x_i, t),$$
 (18)

where $w(x_i,t) = x_{i+1}(t) - x_i(t)$, $x_i(t)$ is the location of fringe (i) at time (t), and $\mathcal{N}_0(x_0,t)$ is the fluid thickness at a zeroth order fringe location (x_0) . For a propagating liquid meniscus, $\mathcal{N}_0(x,t) \geq \delta_0$, where δ_0 corresponds to the absorbed thin-film thickness in the vicinity of the leading edge of the meniscus. Moreover, both the spatiotemporal contours of the meniscus curvature (κ) and curvature gradient $(d\kappa/dx)$ can then be calculated with knowledge of $\mathcal{N}(x,t) - \mathrm{e.g.}$,

$$\kappa(x,t) = \left| \frac{d^2 h}{dx^2} \right| \left(1 + \left(\frac{dh}{dx} \right)^2 \right)^{-3/2}.$$
 (19)

The curvature gradient is an important quantity as it dictates many transient heat and mass transfer phenomena due to its correlation with variations in the surface tension and pressure gradients in the fluid.

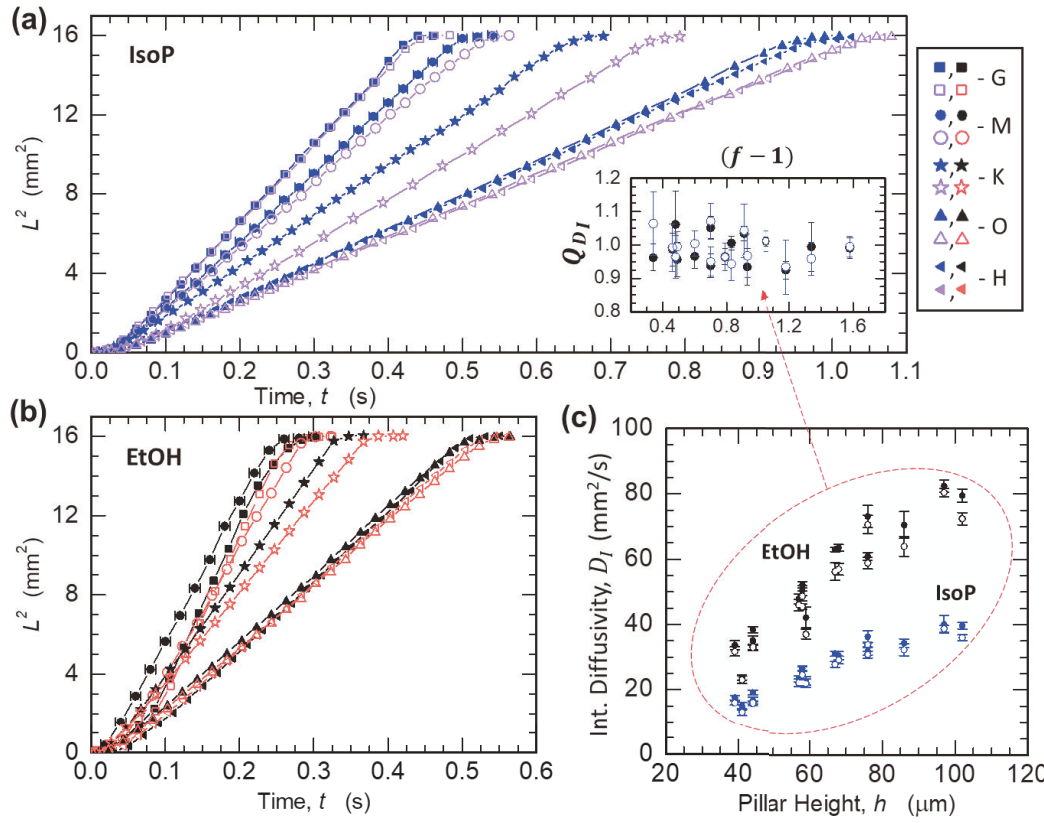


Fig. 6. Anisotropic and diffusion-like hemiwicking behavior. (a) Isopropanol and (b) ethanol spatiotemporal L^2 data for hemiwicking on multiple samples (G, H, K, M, O) and different wicking conventions. The filled- and open-symbols correspond to RA and SC wicking (respectively). Each data set is the average of three independent wicking experiments. Standard error: comparable to the symbol size, see RA data for G in (b). (c) Interface diffusivity as a function of the measured pillar height for all samples (A-P), fluids, and different wicking conventions tested. *Inset plot:* Scaling analysis to evaluate if $v \propto h_p$ (see, Eqs. (6-15)) via the anisotropic interface diffusivity ratio: $Q_{D_I} = D_I^{RA}/D_I^{SC} \times (x_0 - C_1 r)/x_0$, where $C_1 = 0.18$, $x_0^{EtOH} = 24.9$ µm, and $x_0^{IsoP} = 25.1$ µm.

To obtain both the static and the spatiotemporal meniscus extension, the high-speed camera was also setup for both topview and side-view imaging. Fig. 3 provides videography images for both top- and side-view wicking experiments. For static meniscus characterization, typically we use the last row of wetted pillars. Other regions of interest can be viewed; however, other than row-edge effects, the static results in the interior of the wicking array are not of significant interest. Static measurements of x_0 can be acquired using both the top-view and side-view imaging configurations. We note that adopted to define the meniscus extension as the static (or steady-state) extension length: $x_0 \cong x_{\rm p,wall} - \delta_0$. Therefore, measurements of x_0 require establishing a steady-state mode of evaporation within the liquid meniscus (see, Fig. 3a and corresponding inset image).

III. RESULTS AND DISCUSSION

A. Macroscopic Meniscus Propagation

The macroscopic wicking behavior of the hemiwicking samples are observed to have meniscus propagation dynamics that are diffusion-like and one dimensional. Fig. 6 provides the supporting hemiwicking data for this diffusion-like transport. Figs. 6a and 6b plot the meniscus propagation distance (squared) as a function of time - i.e., in accordance with the diffusion relation: $\ell_x^2 = Dt$. For both isopropanol (Fig. 6a) and ethanol (Fig. 6b), after the onset of wicking, there is a relatively short flow acceleration regime (10-50 ms). Then, the meniscus front propagates as \sqrt{t} (or linearly between ℓ_x^2 and t) for multiple samples and the different wicking directions (RA and SC). As shown, RA wicking is faster than SC wicking. Also, liquid ethanol wicks roughly two times faster than isopropanol. Based on Eq. (12), this is expected because $v_{Ca}^{EtOH}/v_{Ca}^{IsoP} \approx 2$. As shown in Figs. 6a and 6b, both wicking directions (relative to the halfconical pillar geometry) exhibit diffusion-like mass transport behavior. We stress that this anisotropic and diffusion-like wicking behavior is found for all our hemiwicking samples (A-P). We have named this type of diffusion-like transport as interface diffusion (D_I) because the hemiwicking process disperses an interface (i.e., the liquid-vapor interface). Table 2 (Appendix) lists the fitted slopes (or D_I values) for all the wicking samples and fluids tested. In further support, Fig. 6c plots all the measured (or fitted) anisotropic values of D_I as a function of pillar height. These data are based analysis of typically three, independent macroscale wicking trials per direction (SC and RA) for each sample (A-P). As discussed in Sec. IIB, we have incorporated the concept of a perceived pillar height (h_p) in our hemiwicking model (see, Eqs. (6-8)), where for RA and SC wicking, $h_p^{RA} \approx h$ and $h_p^{SC} \approx \frac{hx_0}{x_0 + c_1 r}$. As shown in Fig. 6 (inset), if $C_1 \approx 0.18$, then $Q_{D_I} \approx 1$, which corresponds to $D_I^{SC}/D_I^{RA} \approx h_p^{SC}/h_p^{RA} \approx \frac{x_0}{(x_0 + c_1 r)}$.

Experiments in the StS wicking configuration were also conducted; however, the wicking data for StS wicking yielded relativity large systematic errors based on trial-to-trial angle of incidence variations between the pillar array and the liquid pool contact line (or liquid interface normal). Therefore, this manuscript only reports RA and SC wicking data and more studies with StS are needed to both confirm the expected axis-

symmetric, macroscale wicking dynamics (Eq. (11)) and better understand microscale zipping effects.

Interestingly, an interface (or wicking front) diffusivity can be obtained by multiplying the predicted wicking velocity, Eq. (12), by the propagation distance, e.g., $\ell v = \ell \frac{d\ell}{dt}$, and then equating ℓ to the diffusion length for the propagating meniscus front: $\ell = 2\sqrt{D_I t}$. Then, by taking the time derivative of ℓ , the following relationship between the interface diffusivity and the wicking velocity can be derived: $D_I = v\ell/2$. Now, in terms of Eq. (12), the predicted interface diffusivity is

$$D_I = \frac{1}{2} \left(\frac{s}{c_{d0}} \mathbf{v}_{Ca} \right) \ell . \tag{20}$$

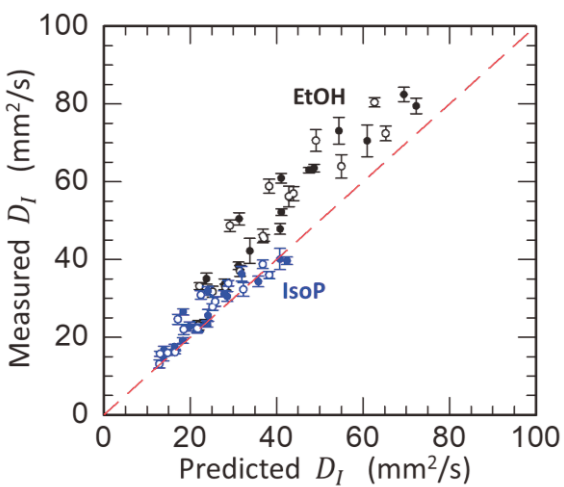


Fig. 7. Comparison between the measured and predicted interface diffusivity (samples A-P). The filled- and open-symbols correspond to RA and SC wicking, where the black- and blue-symbols are for hemiwicking with ethanol and isopropanol (respectively). The dashed red line is a guide to the eye for a 1:1 correlation. The predicted values are based on Eq. (21), using $C_{d0} = 24$ (Stokes), Eqs. (13-14) for K_{\circ} (RA and SC wicking), and $V_{Ca} = 20.1$ m/s and 11.9 m/s ($x_0 = 24.9 \mu m$ and 25.1 μm) for ethanol and isopropanol, respectively.

We note that the solid-liquid Structure factor (S) in Eq. (20) scales inversely with length: therefore, the interface diffusivity in Eq. (20) is predicted to be independent of propagation distance (or time). So, if we rewrite Eq. (20) in terms of the solid-liquid surface texture (K_{\circ}), drag number (C_{d0}), and capillary velocity (v_{Ca}), then we have

$$D_I = \frac{1}{2} \left(\frac{K_{\circ}}{C_{d0}} \right) \mathbf{v}_{\mathsf{Ca}} \,, \tag{21}$$

where $K_{\circ} \propto h/x_0^2$ (see, Eqs. (13-16)). We note that typically the meniscus extension (x_0) is observed to be within the rather narrow range of 15 μ m $\lesssim x_0 \lesssim 30 \ \mu$ m for a variety of different fluids (e.g., isopropanol, ethanol, water, FC70, and isooctane). Therefore, subsequent applications of these predictions (on an ad hoc basis) can assume with $x_0 \simeq 20 \ \mu$ m for other lyophillic wicking fluids. With this said, debates on the practical use of K_{\circ} and how to define and measure x_0 relative to the spatial onset of thin-film absorption regime (δ_0) are needed.

Fig. 7 shows the correlation between our measured and predicted interface diffusivity. The predicted D_I values are based on Eq. (21), using $C_{d0} = 24$ and the appropriate surface texture convention (i.e., Eqs. (13) or (14) for RA or SC wicking, respectively). Thus, the only free parameter in the model predictions is the coupling coefficient C_1 for estimating the perceived pillar height. The correlation between the measured and predicted data is very good. In general, the measured values of the interface diffusivity are greater than the predicted values. Using a drag number of $C_{d0} \leq 14$ yields the opposite result, while $C_{d0} = 19.5$ can be considered the best fit value. We also note that neglecting the $\cos \alpha$ term from the predicted wicking velocity (or solid-liquid surface texture) yielded poor correlations for all samples with $\alpha = 45^{\circ}$.

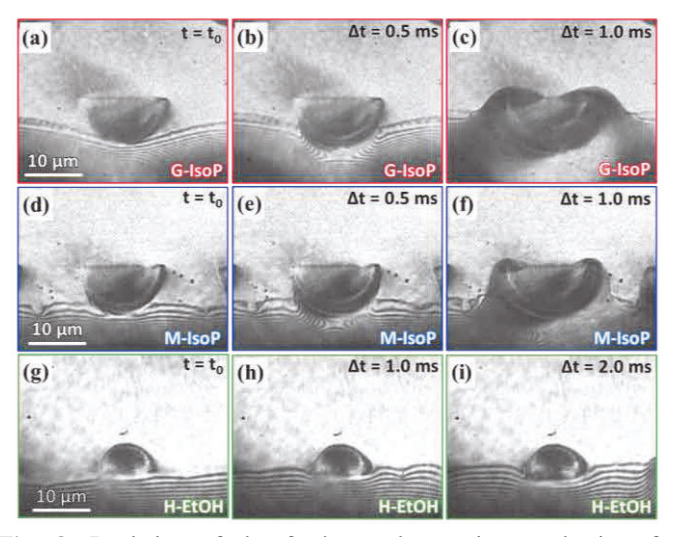


Fig. 8. Depiction of the fundamental pumping mechanism for sustaining hemiwicking flow at the microscale. The microscale pumping mechanism is illustrated via snapshot interferometry images for different samples (G, M, and H), fluids (ethanol and isopropanol), and wicking conventions (RA and SC wicking) in a central region of wicking array ($\ell_x \approx 0.65 \ L$, $\ell_y \approx 0.5 \ W$). Each pillar acts as a fluid pump with the sequential pumping process of (1) fluid-pillar contact, (2) fluid engulfment at the pillar-base, and then (3) vertical (pumping) wicking up the pillar walls.

B. Microscopic Meniscus Propagation

The last section discussed the wicking behavior from a macroscopic perspective based on an averaged wicking front propagation velocity (or interface diffusivity) across an entire row of pillars (or entire row of unit cells). In the following we discuss the wetting behavior from the single pillar and pillar-to-pillar (or microscopic) perspective.

The images in Fig. 8 illustrate the microscopic wetting process. As depicted in Figs. 8a, 8d, and 8g, inter-pillar wicking is initiated by the onset of wetting of a single pillar. The subsequent images for each fluid-sample combination in Fig. 8 illustrate that after meniscus front contact with the pillar-base, then the entire base of the pillar base is engulfed by the fluid. There is some vertical wicking during this engulfment process. However, it is rather sluggish relative to the vertical wicking after engulfment. Thus, after the base of a single pillar is engulfed (or surrounded) by the fluid, then the fluid rapidly

wicks (climbs) up the pillar wall. This fluid climbing process is the key driving (pumping) mechanism for hemiwicking, where in Eqs. (6-8) the pumping pressure (per unit cell) is proportional to the pillar height, surface tension, and pillar spacing relative to the meniscus extension. Thus, each individual pillar drives the propagation of the meniscus front from its pillar base. However, each single pillar pump has a unique spatiotemporal coupling to the surrounding fluid dynamics (i.e., those associated with inertia, drag, and the pumping by neighboring pillars). In this regard, the inter-pillar spacing configuration is critical for facilitating coordinated inter-pillar wetting (climbing).

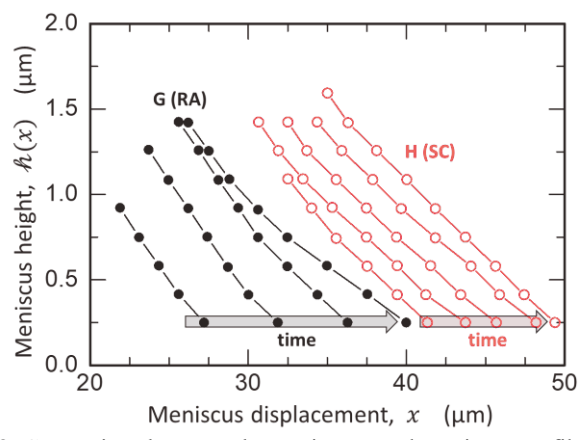


Fig. 9. Comparison between the spatiotemporal meniscus profiles for sample G and sample H during Rapid Ascent (RA) and Sluggish Climb (SC) wicking (respectively) with ethanol. The data is based on interferometry fringe analysis in a central region of wicking array ($\ell_x \approx 0.65 L$, $\ell_y \approx 0.5 W$). Each meniscus profile has temporal increment of 1 ms (sample G: 2.5 to 5.5 ms, sample H: 7.5 to 11.5 ms).

Meniscus stability against a flat face and sharp corner is studied extensively by Jokinen et al., and this stability difference applies here to curved faces in the same way, but simply less pronounced [11]. We stress that if coordinated (or simultaneous) the inter-pillar wetting is frequently occurring, then the corresponding wicking front propagation is more like a plane wave (one dimensional). Moreover, when the wicking front propagation is one dimensional due to near simultaneous interpillar wicking, then we observe a near constant meniscus curvature at leading edge.

Fig. 9 provides spatiotemporal meniscus profile data for this case of pseudo-planewave (one dimensional) meniscus propagation. The data is based on interferometry (fringe) analysis using Eqs. (17-18). The interferometry experiments only provide meniscus profile information during the later stages of inter-pillar wicking (i.e., within $s_x/2 \le x \le s_x$), As illustrated in Figs. 5 and 9, immediately after the pillarengulfment and subsequent wall-wicking processes, there are no visible interferometry fringes due to the large contact angles next to the pillar walls. To circumvent this experimental challenge side-view videography experiments were also conducted. Fig. 10 provides some inter-pillar velocity data. We note that these side-view studies showed significant variability due to edge effects, defect, and debris -- especially for samples with the staggered pillar arrays (A-G). Nevertheless, the velocity data in Fig. 10 illustrates the expected decay in wicking velocity due to the decrease in meniscus curvature.

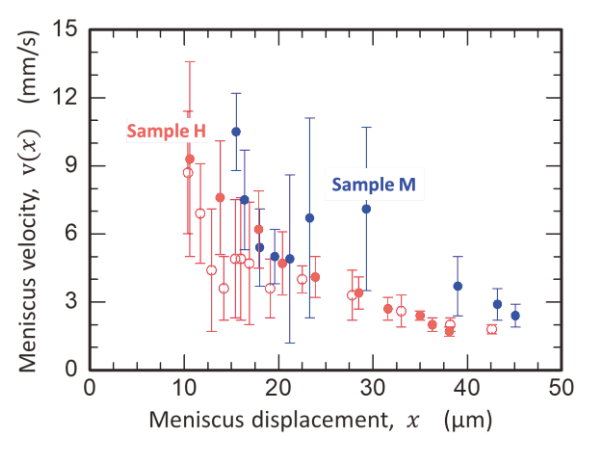


Fig. 10. Inter-pillar velocity distribution for samples M and H. The filled- and open-symbols correspond to RA and SC wicking.

IV. CONCLUSIONS

Microstructured surfaces for enhanced wetting is at the forefront of interfacial heat transport research. This work showed that the anisotropic wicking velocity can be predicted quite reliably at the macroscale. For example, the anisotropic hemiwicking model predicts the interface diffusivity within 20% of that measured experimentally using the Stokes (creeping) flow drag number ($C_{d0} = 24$). An improved model-data correlation ($\lesssim 10\%$) is found using a best fit value of $C_{d0} = 19.5$. At the microscale, however, much more work is needed to understand the spatiotemporal inter-pillar wicking dynamics, which are dictated by a complex interplay between multiple transient processes, such as viscous drag, micro-scale flow vorticity, and coordinated-to-disordered inter-pillar wetting dynamics.

This study can be utilized as a starting point for optimizing wicking arrays with both local (single micro-pillar) and macro-scale anisotropic qualities for tailored flow-fields. In the area of thermal management, future superlyophilic surfaces with high anisotropic qualities can be utilized to create complex flow paths that can direct the fluid flow to specific hot- or cold-spot regions of interest. Anisotropic hemiwicking arrays have applications in a variety of different environments due the feasibility of use with high-temperature refractory metals, alloys, soft materials, and fluids ranging from liquid metals to cryogenic refrigerants. Other areas of application beyond thermal management include water harvesting on superhydrophilic materials and biomimetic materials development [14,15].

V. ACKNOWLEDGEMENTS

The authors acknowledge the helpful discussions with Thomas M. Germain and Tanvir A. Chowdhury. This material is based on research partially sponsored by the National Science Foundation (Grant No. 1653396). The views and conclusions contained herein are those of the authors and should not be interpreted as necessarily representing the official policies or endorsements, either expressed or implied, of the U.S. Government (or departments thereof. Nanolithography fabrication of microstructures, as well as thin film deposition, took place at ORNL Center for Nanophase Material Sciences under User Proposal 2018-329, which is a DOE Office of Science User Facility.

REFERENCES

- [1] T. M. Germain et al., "Measuring Heat Transfer Coefficients for Microchannel Jet Impingement Using Time-domain Thermoreflectance" 2018 17th IEEE Intersociety Conference on Thermal and Thermomechanical Phenomena in Electronic Systems (ITherm), San Diego, CA, 2018, pp. 449-454.
- [2] A. M. Briones et al., "Micrometer-Sized Water Droplet Impingement Dynamics and Evaporation on a Flat Dry Surface" *Langmuir*, vol. 26 Issue 16, pp 13272-13286. July 2010. https://doi.org/10.1021/la101557p
- [3] M. M. Rahma, et al., "Role of Wickability on the Critical Heat Flux of Structured Superhydrophilic Surfaces" *Langmuir*, vol. 30 pp, 11225-11234. Aug 2014. https://doi.org/10.1021/la5030923
- [4] R. Ranjan et al., "Analysis of the Wicking and Thin-Film Evaporation Characteristics of Microstructures" *Journal of Heat Transfer*, vol. 131, Issue 10, pp 101001-101012. Oct. 2009. https://doi.org/10.1115/1.3160538
- [5] J. Bico et al., "Rough wetting" EPL (Europhysics Lett.) vol. 55, no. 2. 2001.(10.1209/epl/i2001-00402-x/pdf)
- [6] Z. Li, F. Yang, Y. Yin, "Smart Materials by Nanoscale Magnetic Assembly" *Advanced Functional Materials*, Vol. 30, Issue 2. July 2019. https://doi.org/10.1002/adfm.201903467\
- [7] S. R. Krishnan et al., "A simple analytic model for predicting the wicking velocity in micropillar arrays' *Sci. Reports*, vol 9. No. 20074. Dec. 2019. https://doi.org/10.1038/s41598-019-56361-7
- [8] J. Kim et al., "Dynamics of hemiwicking" *J. Fluid Mech.* Vol. 800, pp 57-71. June 2016. Accessed on Mar. 1, 2020. https://doi.org/10.1017/jfm.2016.386
- [9] D. Xia et al., "Anisotropic Wetting Surfaces with One-Dimesional and Directional Structures: Fabrication Approaches, Wetting Properties and Potential Applications" *Advanced Materials*, vol. 24 issue 10, pp 1287-1302, Feb. 2012. https://doi.org/10.1002/adma.201104618
- [10] J. Feng, J. Rothstein, "One-way wicking in open microchannels controlled by channel topography", *Journal of Colloid and Interface Science*, vol. 404, pp. 169-178, 2013. DOI:10.1016/jcis.2013.02.052.
- [11] V. Jokinen et al., "Microstructured Surfaces for Directional Wetting" *Advanced Materials*, vol. 21 issue 47, pp 4835-4838, Dec. 2009. DOI: 10.1002/adma.200901171
- [12] A. A. Arends et al., "Simultaneous reflectometry and interferometry for measuring thin-film thickness and curvature". *AIP Review of Scientific Instruments*, vol. 89, iss. 5, May 2018. https://doi.org/10.1063/1.5021704
- [13] S. A. Putnam et al, "Microdroplet evaporation on superheated surfaces." *Int. J Heat Mass Transf.* vol. 55, pp. 5793-5807 2011. doi:10.1016/j.ijheatmasstransfer.2012.05.076
- [14] A. Lee, M. Moon, H. Lim, W. Kim, and H. Kim, "Water harvest via dewing" *Langmuir*, vol 28, pp 10183-10191 2012. https://doi.org/10.1021/la3013987
- [15] K. Koch and W. Barthlott, "Superhydrophobic and superhydrophilic plant surfaces: an inspiration for biomimetic materials" Phil. Trans. Royal Society A, vol .367 Issue 1893. April 2009. https://doi.org/10.1098/rsta.2009.0022

Table 1. Anisotropic Pillar Geometry and Spacing. $s_r \quad s_v \quad r \quad \alpha \quad h \quad h_m \quad f$

| | s_x | s_y | r | α | h | h_m | f |
|------------------|-------|-------|------|-----|------|-------|------|
| | (µm) | (µm) | (µm) | (°) | (µm) | (µm) | , |
| \boldsymbol{A} | 40 | 80 | 10 | 45 | 50 | 41 | 1.34 |
| В | 40 | 80 | 10 | 45 | 70 | 59 | 1.48 |
| \boldsymbol{C} | 40 | 80 | 10 | 45 | 90 | 71 | 1.57 |
| D | 40 | 80 | 15 | 45 | 60 | 57 | 1.70 |
| E | 40 | 80 | 15 | 45 | 75 | 68 | 1.83 |
| F | 40 | 80 | 15 | 45 | 90 | 76 | 1.93 |
| \boldsymbol{G} | 40 | 80 | 15 | 45 | 105 | 97 | 2.18 |
| \boldsymbol{H} | 50 | 50 | 10 | 0 | 50 | 44 | 1.46 |
| I | 50 | 50 | 10 | 0 | 70 | 58 | 1.60 |
| \boldsymbol{J} | 50 | 50 | 10 | 0 | 90 | 76 | 1.79 |
| K | 50 | 50 | 15 | 0 | 60 | 58 | 1.91 |
| \boldsymbol{L} | 50 | 50 | 15 | 0 | 75 | 67 | 2.05 |
| M | 50 | 50 | 15 | 0 | 90 | 86 | 2.34 |
| N | 50 | 50 | 15 | 0 | 105 | 102 | 2.58 |
| 0 | 40 | 80 | 15 | 45 | 45 | 39 | 1.49 |
| P | 50 | 50 | 15 | 0 | 45 | 44 | 1.70 |

Table 2. Interface Diffusivities $(D_I \pm \Delta D_I)$ for Anisotropic Hemiwicking with Ethanol and Isopropanol.

| | Ethanol | | | | Isopropanol | | | | |
|------------------|----------------|------------|----------------------|-------------------|----------------|------------|-------------------|-------------------|--|
| | $D_I^{\rm RA}$ | D_I^{SC} | $\Delta D_I^{ m RA}$ | ΔD_I^{SC} | $D_I^{\rm RA}$ | D_I^{SC} | ΔD_I^{RA} | ΔD_I^{SC} | |
| | (mm^2/s) | (mm^2/s) | (mm^2/s) | (mm^2/s) | (mm^2/s) | (mm^2/s) | (mm^2/s) | (mm^2/s) | |
| A | 23.78 | 23.05 | 0.90 | 1.27 | 14.95 | 13.11 | 1.09 | 1.05 | |
| \boldsymbol{B} | 42.19 | 37.06 | 3.33 | 1.41 | 22.74 | 22.01 | 1.22 | 1.30 | |
| \overline{C} | 58.52 | 52.97 | 2.18 | 1.95 | 29.67 | 28.82 | 1.89 | 1.34 | |
| D | 47.86 | 46.05 | 1.40 | 1.74 | 23.40 | 22.25 | 0.84 | 1.13 | |
| \boldsymbol{E} | 63.50 | 56.96 | 0.99 | 1.83 | 30.47 | 29.17 | 1.26 | 1.18 | |
| \overline{F} | 73.10 | 70.59 | 3.42 | 2.82 | 36.29 | 33.86 | 1.89 | 0.71 | |
| G | 82.44 | 80.42 | 1.82 | 1.20 | 40.09 | 38.74 | 2.73 | 1.09 | |
| H | 35.05 | 33.12 | 1.42 | 0.87 | 16.73 | 15.74 | 0.97 | 0.67 | |
| I | 50.45 | 48.71 | 1.55 | 1.51 | 26.48 | 24.61 | 0.80 | 1.30 | |
| \boldsymbol{J} | 60.89 | 58.84 | 1.22 | 1.78 | 31.89 | 30.86 | 1.13 | 1.05 | |
| K | 52.19 | 45.51 | 0.85 | 0.83 | 25.61 | 22.18 | 1.55 | 0.79 | |
| L | 62.98 | 56.22 | 1.15 | 2.64 | 31.14 | 27.80 | 0.76 | 0.84 | |
| M | 70.51 | 63.96 | 4.08 | 3.04 | 34.31 | 32.29 | 1.37 | 1.79 | |
| N | 79.50 | 72.42 | 1.99 | 1.90 | 39.66 | 36.00 | 0.97 | 0.92 | |
| 0 | 33.61 | 31.70 | 1.39 | 1.41 | 17.58 | 15.96 | 0.64 | 0.66 | |
| P | 38.35 | 32.89 | 0.96 | 0.90 | 19.15 | 16.14 | 0.76 | 0.42 | |